Available online at www.sciencedirect.com
SCIENCE DIRECT®
Deep-Sea Research I 51 (2004) 367–381
DEEP-SEA RESEARCH PART I
www.elsevier.com/locate/dsr

Winter geostrophic currents and eddies in the western Iberia coastal transition zone

Paulo B. Oliveira[a,*], Álvaro Peliz[a], Jesús Dubert[b], Teresa L. Rosa[a], A. Miguel P. Santos[a]

[a] *IPIMAR, Av. Brasilia, Lisboa 1449-006, Portugal*
[b] *Department of Physics, University of Aveiro, Aveiro 3810-193, Portugal*

Received 7 October 2002; received in revised form 19 March 2003; accepted 9 October 2003

Abstract

The results of a fine-resolution hydrological survey conducted in the western Iberia coastal transition zone in February 2000 are used to describe the vertical structure of the density field and geostrophic currents in the Central Water (CW) layer. The vertical density distribution was characterized by the presence of three pycnocline layers: (i) at the surface driven by the buoyancy input of a low-salinity plume, (ii) at about 200 m ($\sigma_\theta = 27.0$), below the surface mixed layer and, (iii) in the transition layer between the Central and Mediterranean Water at depths close to 600 m ($\sigma_\theta = 27.3$). It is shown that the density distribution at the depth of the deeper pycnocline controls much of the geopotential anomaly field when the reference level is below the lower Mediterranean Water core ($\simeq 1200$ m), leading to a high sensitivity in the geostrophic velocity profiles to the choice of the reference level. The use of a reference level above 600 m artificially reduces the flow in the lower CW layer ($27.0 < \sigma_\theta < 27.3$) where significant volume transports are found when a reference level at 1400 dbar is used. In particular, the presence of an equatorward flow at about 400 m in the near-slope region at 41°N was found to be responsible for the volume transport of 0.3 Sv in the direction opposite to the same volume transport in the upper CW layer ($\sigma_\theta < 27.0$), a feature not reported in previous studies based on field data. In the northernmost sections, the flow in the lower CW layer was directed in the same poleward direction as the upper layer in the near-slope region, leading to a deep signature in the poleward current with a maximum volume transport increase from 0.5 Sv in the upper CW layer to 1.1 Sv in both the layers. Schematic views of the non-divergent circulation in two isopycnal CW layers are used to present the main flow paths and volume transports associated with the mesoscale eddy field.

Keywords: Mesoscale eddies; Coastal Transition Zone; Geostrophic currents; Northeast Atlantic; Iberian Peninsula; Portugal; 40–42°N; 10–8°W

1. Introduction

The circulation off western Iberia is characterized by a complex current system subjected to strong seasonality and mesoscale variability, showing reversing patterns between summer and

*Corresponding author. Fax: +351-213-015-948.
E-mail address: pbo@ipimar.pt (P.B. Oliveira).

0967-0637/$ - see front matter © 2003 Elsevier Ltd. All rights reserved.
doi:10.1016/j.dsr.2003.10.016

winter in the upper layers of the slope/outer shelf area (e.g., Ambar and Fiúza, 1994; Barton, 1998). In spite of an increasing number of studies focusing on this eastern oceanic boundary layer, very few detailed field studies specifically dedicated to the investigation of wintertime circulation have been published.

Most of the present knowledge of the circulation in the upper layers in this season is based on the works of Frouin et al. (1990) and Haynes and Barton (1990). They reported the presence of a poleward current along the coast of NW Iberia, generally described as a narrow poleward flow along the upper slope/shelf break zone, transporting warm and salty waters in the upper 200–300 m during autumn and winter. Further evidence of a net poleward flow of Central Water (CW) was presented by Mazé et al. (1997). In their study of the volume budget off the Iberian Peninsula, the authors reported an estimate of a northward volume transport higher than $10^6\ m^3\ s^{-1}$ in the slope region at 43°N, and discussed their findings with regard to the notion of a southward Portugal Current, proposing seasonality of the eastern boundary processes as an explanation for the apparent contradiction. In addition to its seasonal character, it has also been shown that the poleward current is affected by considerable mesoscale activity (e.g., Haynes and Barton, 1990; Dubert, 1998; Fiúza et al., 1998; Peliz et al., 2003b). The importance of the mesoscale activity in the ventilation of the different modes of the Eastern North Atlantic Central Water (ENACW) was evaluated by Pérez et al. (2001), who pointed to mesoscale eddies as the main mechanism for the downstream indirect ventilation of ENACW of subtropical origin.

An element of additional complexity of the flow field off West Iberia is the vertical coupling between the Central and Mediterranean Water masses. Evidence of circulation features extending from the surface down to Mediterranean Water levels has been obtained from combination of in situ and satellite infrared images (Pingree and Le Cann, 1993; Pingree, 1995; Oliveira et al., 2000), from comparisons between satellite-derived sea surface height and dynamic topography (Stammer et al., 1991), by the identification of similarities between the zonal distribution of the transports in Central and Mediterranean water layers (Mazé et al., 1997), and from the vertical distribution of chemical fields (Pérez et al., 2001). These previous works prompted us to undertake a careful analysis of the vertical structure of the flow field in order to improve our understanding of the complex current system in the western Iberia coastal transition zone (CTZ).

The aim of this paper is to describe the vertical structure of the geostrophic currents and volume transports of the mesoscale off-slope eddies at CW levels, based on the results from a fine-resolution conductivity–temperature–depth (CTD) survey conducted off the NW Portuguese coast in February 2000. First, mean vertical profiles of selected parameters are used to show the presence and locate the depths of pycnocline layers and to relate them with the water masses found in the region. Second, horizontal maps of the thermohaline and density fields at the levels of the identified subsurface pycnoclines are presented to characterize the areas of maximum zonal density gradient that, in turn, control the position and shape of the main circulation features. Finally, a description of the mesoscale eddy field and associated transports using different reference levels are presented and discussed using individual velocity profiles computed between selected station pairs, maps of geopotential anomaly and vertical sections of geostrophic velocity.

2. Data

The SURVIVAL'2000 cruise was conducted off western Iberia in the framework of project SURVIVAL—"Assessing the Impact of Hydrodynamic Forcing on the Survival of Small Pelagic Fish Early Life Stages of western Iberia". It was carried out from 16 to 21 February on board R.V. *Noruega* and included hydrographic and zooplankton sampling stations (Santos, 2000). The sampling area of the larger-scale CTD survey extended from nearshore to 10°W, corresponding to a distance of about 140 km off the coast (Fig. 1). A total of 78 stations, with a zonal spacing ranging from 5 km at shallower depths to

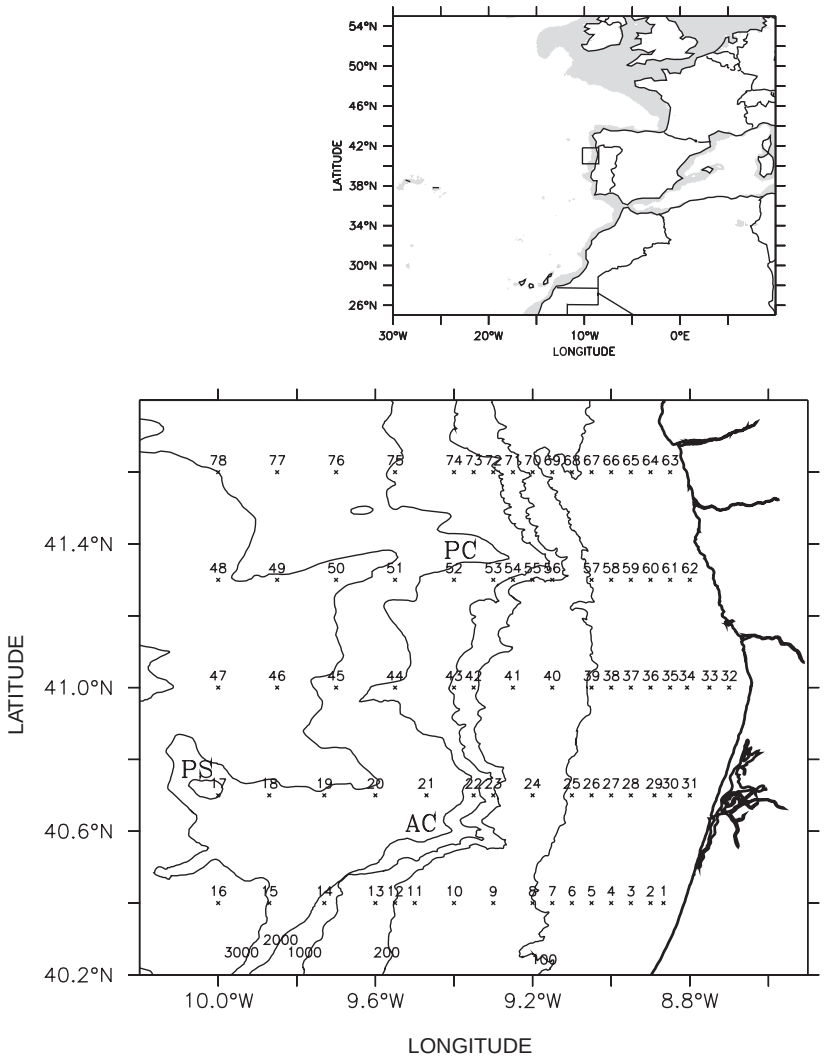

Fig. 1. Map of CTD stations off western Iberia shelf and slope occupied during the cruise SURVIVAL'2000 from 16 to 21 February 2000 on board R.V. *Noruega*. The main topographic features are identified as follows: PS—Porto seamount, AC—Aveiro Canyon and PC—Porto Canyon.

15 km offshore, were occupied along five zonal sections extending from 40.4°N to 41.6°N with a meridional spacing of about 30 km, covering a total alongshore distance of about 130 km. The main topographic features in the region are the Aveiro Canyon at 40.7°W, the Porto Canyon near 41.3°W and the Porto Seamount at about 40.7°N, 10°W.

A SeaBird 9p CTD instrument with a selected sampling rate of 12–24 scans/s^{-1} was used to measure vertical profiles of conductivity and temperature. The profiles were obtained down to the near bottom for depths less than 1400 m; at deeper stations they reached generally 1400 m, with the exception of stations 44–47, where maximum depth exceeded 1800 m. Lowering speed was kept as close as possible to 1 m s^{-1}. Water samples were collected for calibration and salinity was measured in the laboratory with a Guildline Autosal 8400B Salinometer. Standard algorithms (Fofonoff and Millard, 1983) were used to compute derived quantities such as salinity,

density and geopotential anomalies. Geostrophic currents were computed using several reference levels in order to analyze the differences in the resulting flow patterns and associated transports. The extrapolation approach of Reid and Mantyla (1976) was used for depths shallower than the reference level.

3. Results

3.1. Mean vertical structure

The main features of the vertical distribution of observed hydrological fields and derived properties are first described using vertical profiles of horizontally averaged temperature, salinity, potential density anomaly σ_θ ($\rho(S,\theta,0)-1000$) and buoyancy frequency ($N^2=-(g/\rho)\partial\sigma_\theta/\partial z$) presented in Fig. 2. Mean temperature, salinity and σ_θ values (solid lines) are enclosed by minimum and maximum profiles resulting from averaging the eight (10% of total casts) lowest and highest values for each depth level. These enveloping profiles are thus indicative of the horizontal variability of the hydrological fields at each depth. Vertical gradients of the mean temperature ($\partial T/\partial z$) and salinity ($\partial S/\partial z$), smoothed with a boxcar window of 75 dbar width, are superimposed. The vertical profile of the horizontally

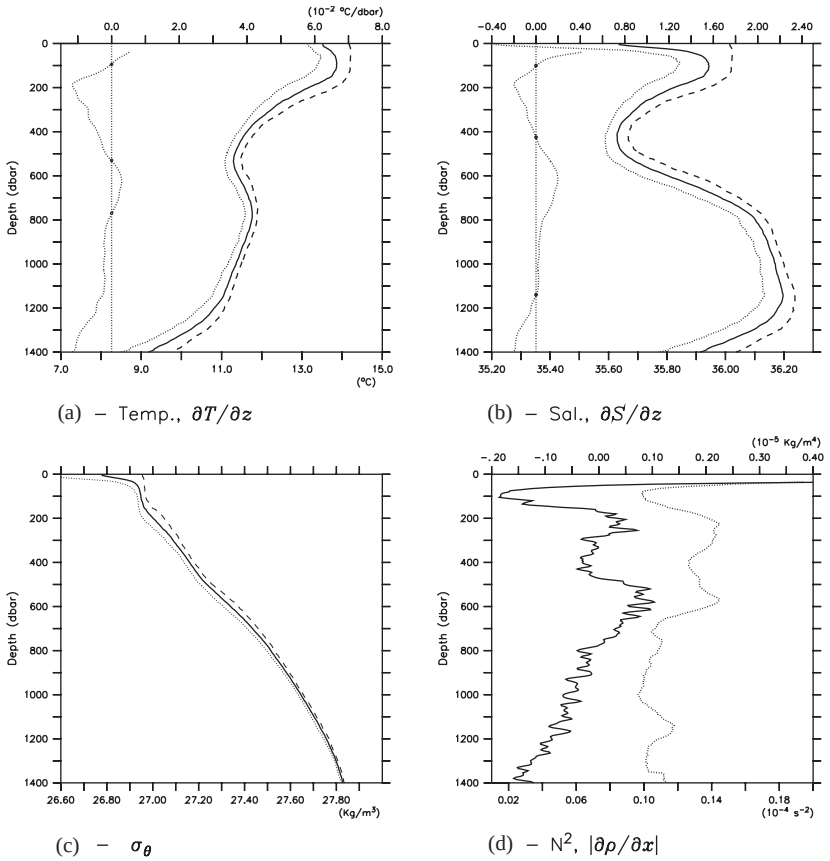

Fig. 2. Vertical profiles of horizontally averaged summary statistics of (a) temperature, (b) salinity and (c) σ_θ. Solid lines represent average values, enveloping maximum and minimum values are represented by dashed and dotted lines. Profiles of smoothed vertical gradients of average temperature $\partial T/\partial z$ (10^{-2}°C dbar^{-1}, top axis) and salinity $\partial S/\partial z$ (10^{-2} dbar^{-1}, top axis) are superimposed as dotted lines on the left of (a) and (b). (d) Buoyancy frequency N^2 (10^{-4} s^{-2}, solid line) and zonal density gradient $|\partial\rho/\partial x|$ (10^{-5} kg m^{-4}, top axis, dotted line).

averaged absolute values of the zonal density gradient ($|\partial\rho/\partial x|$), smoothed with the same operator, is shown with the mean buoyancy frequency profile in Fig. 2d. To relate the observed profiles and the water masses at different density levels, a θ/S scatter plot of all CTD casts for depths greater than 50 dbar is presented in Fig. 3.

The mean temperature and salinity profiles are similarly shaped, presenting three zero crossings in their vertical gradients: (i) at about 100 dbar, (ii) in the depth range of 400–600 dbar and (iii) below 700 dbar corresponding, respectively, to the winter mixed layer, the minimum values at the lower edge of the CW and the maximum values associated with the Mediterranean Water cores.

Above the winter mixed layer, an absolute minimum in the buoyancy frequency between 50 and 150 dbar is clearly identifiable (Fig. 2d), corresponding to a sharp salinity decrease that creates a strong pycnocline in the top 50 dbar of the water column (Fig. 2c). This low-salinity buoyant plume is found all year-round off the west coast of the Iberian Peninsula (e.g., Fiúza and Sousa, 1989; John et al., 1996; Fiúza et al., 1998; Peliz et al., 2002), and was named Western Iberia Buoyant Plume (WIBP) by Peliz et al. (2002). From Figs. 2b and c, the WIBP can be characterized from present data by values of $\sigma_\theta < 26.9$ (6–80 dbar), occupying the top 50 m of the water column. Since the purpose of this work is the description of the mesoscale structure of off-slope circulation at CW depths, based on the spatial density distribution (assuming the geostrophic balance), the results presented here are focused on the observations below the buoyant plume where both the low-density values and the ageostrophic Ekman drift are expected to play a major role in its dynamics. A description of the WIBP with this set of observations, including its impact on the retention of sardine eggs and larvae, is found in Santos et al. (2004).

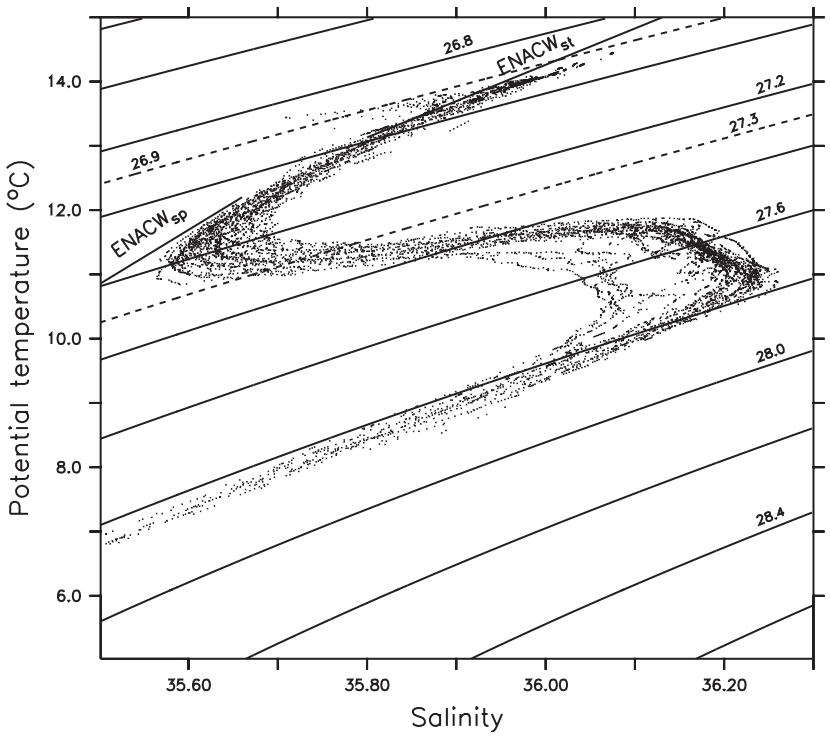

Fig. 3. θ/S scatter plot of all CTD casts for depths below 50 dbar. The θ/S reference lines of ENACW as in Ríos et al. (1992) are also shown.

Below the winter mixed layer centered at 100 dbar, the temperature and salinity gradually decrease down to 530 and 425 dbar, respectively, with maximum vertical gradients at about 200 dbar, corresponding to the depth of a pycnocline represented as a relative maximum in the buoyancy frequency profile (Fig. 2d). In addition to this pycnocline at the depth of $\sigma_\theta = 27.0$ (138–272 dbar), another layer of buoyancy frequency increase can be clearly identified at about 600 dbar, where $\sigma_\theta = 27.3$ (520–633 dbar). These depths correspond to the layers of the ENACW (e.g., Fiúza et al., 1998) and the transition layer between ENACW and the Mediterranean Water (Ambar and Howe, 1979), respectively (Fig. 3).

It is worth noting that it is also at the depths of 200 and 600 dbar that relative maxima of the zonal density gradient $|\partial\rho/\partial x|$ are found (Fig. 2d), indicating a vertical wandering of these pycnocline layers which, from the thermal wind equations, are the locus of maximum vertical shear of the meridional geostrophic velocity component, governing many of the observed features of the geostrophic flow as will be shown in the next sections.

3.2. Horizontal distributions at pycnocline layers

The horizontal distributions of temperature, salinity and σ_θ centered at 200 and 600 dbar (Figs. 4a–f) reveal that most of the spatial variability at those depths is governed by the presence of colder and fresher water (shaded areas in Figs. 4a–d) in the northwestern region of the surveyed area, with absolute minimum values located at about 41°N, 9.7°W, contrasting with the warmer and saltier waters in the southern slope region.

At 200 dbar, the region of lower temperature and salinity (shaded areas correspond to values of $\theta < 12.8$°C, $S < 35.80$ and $|\partial\rho/\partial x| > 0.25 \times 10^{-5}$ kg m^{-4}) extends meridionally in a tongue-like southward intrusion, with its axis at 9.7°W, and bounded to the east by a strong thermohaline front separating it from the warmer and saltier waters found at the slope. This colder and fresher water intrusion is denser than its surroundings because at this level, the temperature effect on density prevails over the salinity effect. In other words, the density contrast between the northern offshore waters and the upper slope waters is essentially thermally driven. The waters in the slope region are generally lighter than offshore, with the exception of the southernmost section, where a local temperature minimum in the stations close to the shelf break leads to a reversal of zonal density gradient in the southern boundary.

The areas of maximum absolute zonal density gradient (shaded areas in Fig. 4e, $|\partial\rho/\partial x| > 0.25 \times 10^{-5}$ kg m^{-4}) are found to the east and west of the axis of the cold tongue, along 9.7°W. From the thermal wind equations, considering the layers below 200 m at rest, the areas west of 9.7°W would correspond to southward flow, whereas the areas to the east would correspond to a northward flow. The circulation pattern associated with the density distribution would be a cyclonic meander extending south to about 40.8°N. Warm and saltier waters entering the surveyed area from southwest would be transported inshore just south of 40.7°N, turning poleward between 9.7°W and 9.6°W and flowing close to the slope and leaving the area in the northernmost section. However, this pattern is significantly modified as a result of the strong vertical shear in the lower levels, namely at 600 dbar.

At 600 dbar, the area occupied by relatively cold and fresh water, with $\theta < 11.2$°C and $S < 35.80$ (shaded areas in Figs. 4b and d), shows basically the same eastern and southern limits as at the 200 dbar level (Figs. 4a and c), but extends further to the west at 41.3°N corresponding to an offshore decrease in temperature and salinity. The density field at 600 dbar (Fig. 4f) parallels the temperature and salinity fields in a similar way to the level of 200 dbar. However, at 600 dbar the salinity effect on density prevails over the effect of temperature, and the regions filled with lighter waters correspond to low-salinity anomalies. This leads to opposite vertical shears in the geostrophic velocity in the two layers. Assuming that the layers below 600 dbar were at rest and there are no horizontal density gradients in the upper layers, the circulation above 600 dbar would be dominated by the presence of an anti-cyclonic eddy centered at the local density minimum, at 41°N, 9.7°W, and two counter-rotating mesoscale structures to the west,

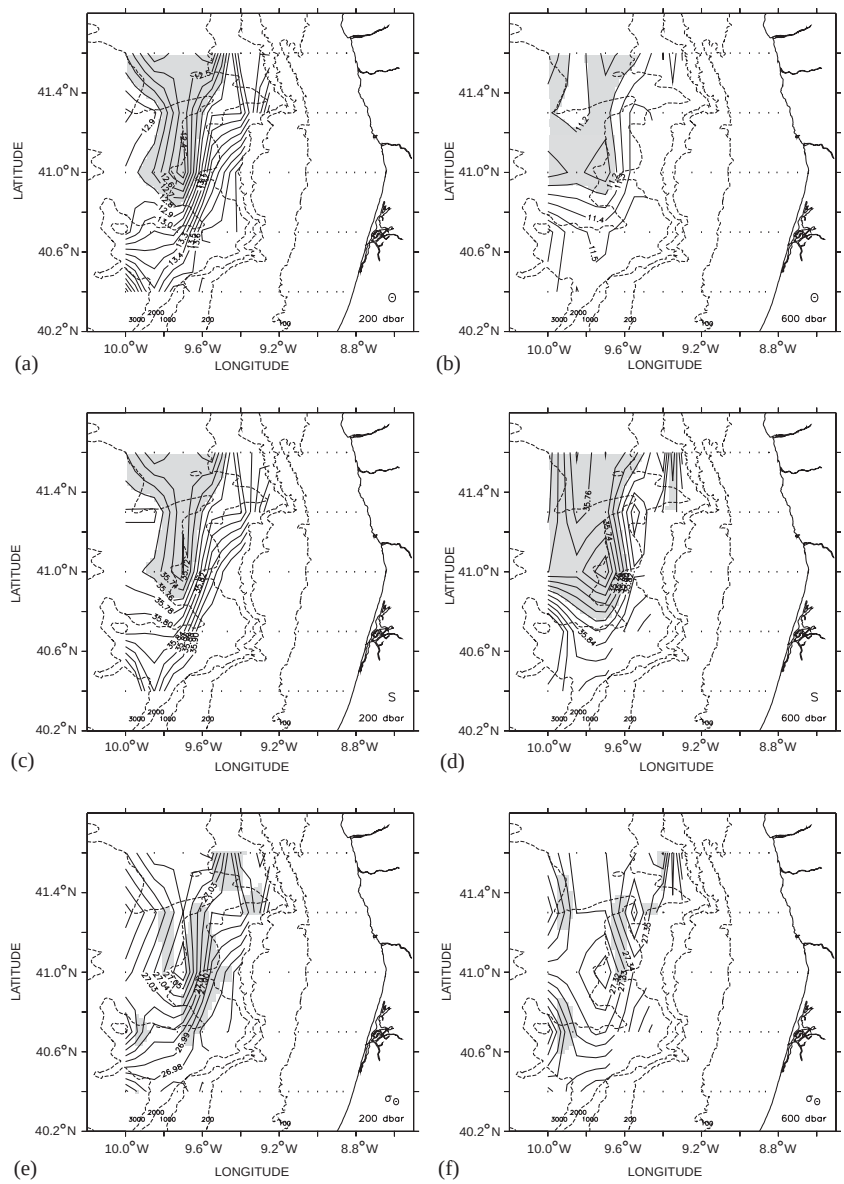

Fig. 4. Horizontal distributions of potential temperature θ (°C), salinity and σ_θ at 200 dbar (left, shaded areas: $\theta < 12.8$°C, $S < 35.76$ and $|\partial\rho/\partial x| > 0.25 \times 10^{-5}$ kg m^{-4}) and 600 dbar (right, shaded areas: $\theta < 11.2$°C and $S < 35.80$ and $|\partial\rho/\partial x| > 0.25 \times 10^{-5}$ kg m^{-4}).

centered at 40.7°N and 41.3°N, creating a confluence zone close to 41°N. At 41.3°N, a small-scale density maximum associated with a positive salinity anomaly at 9.55°W, would correspond to a cyclone inducing a northward flow attached to the slope, continuing further north as a result of the narrow band of lighter (fresher) waters crossing the Porto Canyon.

3.3. Geostrophic currents

Vertical profiles of geostrophic velocity were computed to evaluate the sensitivity of the geostrophic currents to the choice of different reference levels, in a region characterized by strong horizontal density gradients at pycnocline depths associated with mesoscale structures with length

scales of O (10 km). Fig. 5 shows the resulting vertical profiles computed using pairs of the four offshore stations of the zonal transect at 41°N and three reference levels. The 350 dbar level was used to compare the results with the previous studies that used similar reference levels (e.g., Frouin et al., 1990; Fiúza et al., 1998). The 1000 dbar level was selected to illustrate the results when the reference is at the level dominated by the Mediterranean Water flow, despite being a level of a minimum zonal density gradient as shown in Fig. 2d. Finally, the 1400 dbar level was chosen because it was the deepest common level for off-slope stations and therefore could be used to produce maps of dynamic height field from the available station data.

The resulting velocity profiles show remarkable differences in the intensity of the flow at various depths as a result of the position of each station pair relative to the density structures presented in Figs. 4e and f. In particular, the strong and opposite vertical shears above 400 dbar shown in Figs. 5a and c can readily be linked to the opposite zonal density gradients along 41°N at 200 dbar shown in Fig. 4e. The same is true when the vertical shear below 400 dbar (Figs. 5b and c) is compared with the density gradient at 600 dbar (Fig. 4f).

Despite the differences of the absolute velocity values, all velocity profiles show small vertical shears at depths greater than 1400 dbar, an expected feature for depths below the deep Mediterranean Water core. However, in addition to a small vertical shear, it is also expected that the absolute velocity values should be small in the deeper layers (e.g., Mazé et al., 1997), a feature that is not observed in the velocity profiles computed with reference levels at 350 and 1000 dbar. A qualitative criterion, based on the velocities calculated for depths larger than 1400 m, is therefore used for the validation/rejection of the reference levels. From the velocity profiles obtained with the reference level at 1400 dbar an "error" interval of $\pm 3\ \mathrm{cm\ s^{-1}}$ in the deepest layers (shaded band in Fig. 5) is adopted for the geostrophic velocity estimates, as well as for the transport calculations presented below.

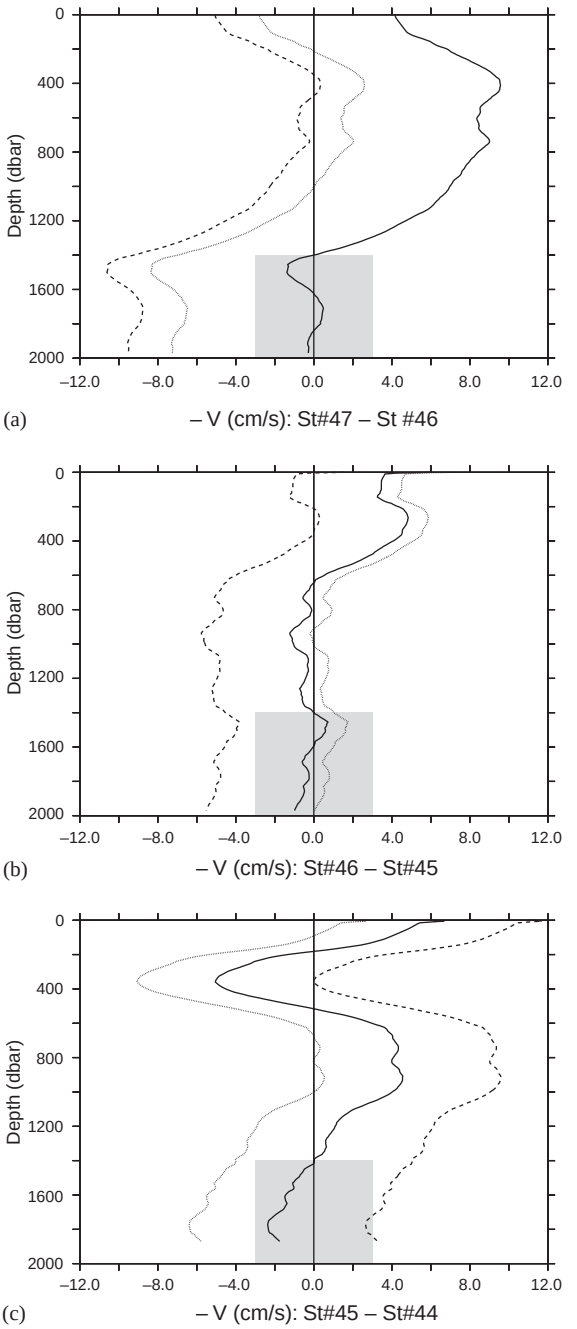

Fig. 5. Meridional geostrophic velocity component computed from dynamic height difference of consecutive stations using reference levels at 1400 dbar (solid), 1000 dbar (dotted) and 350 dbar (dashed). Gray bar illustrates the width of the $3\ \mathrm{cm\ s^{-1}}$ interval.

It should be noted that in almost all velocity profiles calculated with reference levels at 350 and 1000 dbar, the velocity values at depths close to 2000 m fall out of the $\pm 3\ cm\ s^{-1}$ interval. In particular, the use of a reference level close to 400 dbar, where relative maximum and minimum velocity values occur, leads to absolute velocity values exceeding $10\ cm\ s^{-1}$ at 1500 dbar (Fig. 5a) and a 1200 m deep water column flowing in the same direction with velocities exceeding $4\ cm\ s^{-1}$ (Fig. 5b). The use of a reference level at 1000 dbar, at a depth of the minimum zonal density gradient, is also inadequate given the important vertical shears in the depth range 1000–1400 dbar (Figs. 5a and c). In view of the selected criteria, the results of the geostrophic calculations obtained with the 350 dbar reference level are not better than those obtained with the 1000 dbar level. However, because of its frequent use in the literature, the level of 350 dbar is retained for comparison to the following geostrophic estimates and transport calculations.

The velocity profile computed from the dynamic height difference between the near-slope stations 44 and 45 (Fig. 5c), with the reference level at 1400 dbar, shows the presence of equatorward flow at 400 dbar resulting from the strong vertical decrease of the velocity values above 600 dbar. This is a conspicuous feature of the flow field found in vertical sections of the meridional geostrophic velocity component computed with the reference level at 1400 dbar (Fig. 6, right). This undercurrent is associated with a reversal of the isopycnal orientation close to the slope at depths below the poleward slope current. With shallower reference levels (350 dbar) it is artificially removed from the geostrophic velocity field (Fig. 6, left). Another remarkable difference in the vertical sections presented in Fig. 6 is the vertical extension of some flow features, namely the poleward flow in the near-slope region at 41.3°N and 41.6°N and offshore at 40.7°N and 41.0°N.

3.4. Circulation structures and volume transports

The meridional volume transports in the CW layers computed from the velocity sections presented in Fig. 6 are summarized in Table 1. Two isopycnal layers were selected: (i) the upper CW layer (surf.), defined by $\sigma_\theta < 27.0$, above the 200 dbar pycnocline and (ii) the lower CW layer (mid.), defined by $27.0 < \sigma_\theta < 27.3$, between the 200 and 600 dbar pycnoclines. Interval estimates were calculated with the error interval of $\pm 3\ cm\ s^{-1}$ discussed above.

Poleward transports in the upper layer (Table 1), for both reference levels are very similar, despite the differences in the zonal distribution of the poleward flow in the upper 200 dbar displayed in Fig. 6. The greater discrepancies are in the mid-depth layer ($27.0 < \sigma_\theta < 27.3$) as a result of the necessarily low-velocity values when the reference level at 350 dbar is used. In this layer, some values of the poleward transport computed with the reference level at 1400 dbar are more than double those obtained with the 350 dbar reference level. The equatorward volume transports computed with the 350 dbar reference level are all less than 0.3 Sv. On the other hand, most of the values computed with the 1400 dbar reference level are greater than or equal to 0.3 Sv reaching values as high as 0.9 Sv at mid-depth in the northernmost section.

The absence of a poleward flow at the southernmost section, the strong equatorward flow both at the northern and southern sections and the vanishing equatorward transports at different latitudes (40.7°N and 40.4°N—350 dbar, 41°N—1400 dbar), indicate the presence of significant volume exchanges at the western boundary of the study region. Areas of recirculation can also be identified in the maps of geopotential anomaly and corresponding geostrophic velocity vectors, at the levels of 400 and 100 dbar (Fig. 7). The depths of 400 and 100 dbar were selected as representative of the main flow cores shown in Fig. 6. To aid the description of the main features of the geostrophic circulation, the regions where the currents display an anticyclonic or cyclonic rotation are labeled Ai_d or Ci_d, respectively, where i is an occurrence number increasing northward, and d is depth. For convenience, these regions are referred to as cyclonic and anticyclonic features, although they do not necessarily correspond to closed eddies.

The map of the dynamic height at 400 dbar referenced to 1400 dbar (Fig. 7a) is similar to the

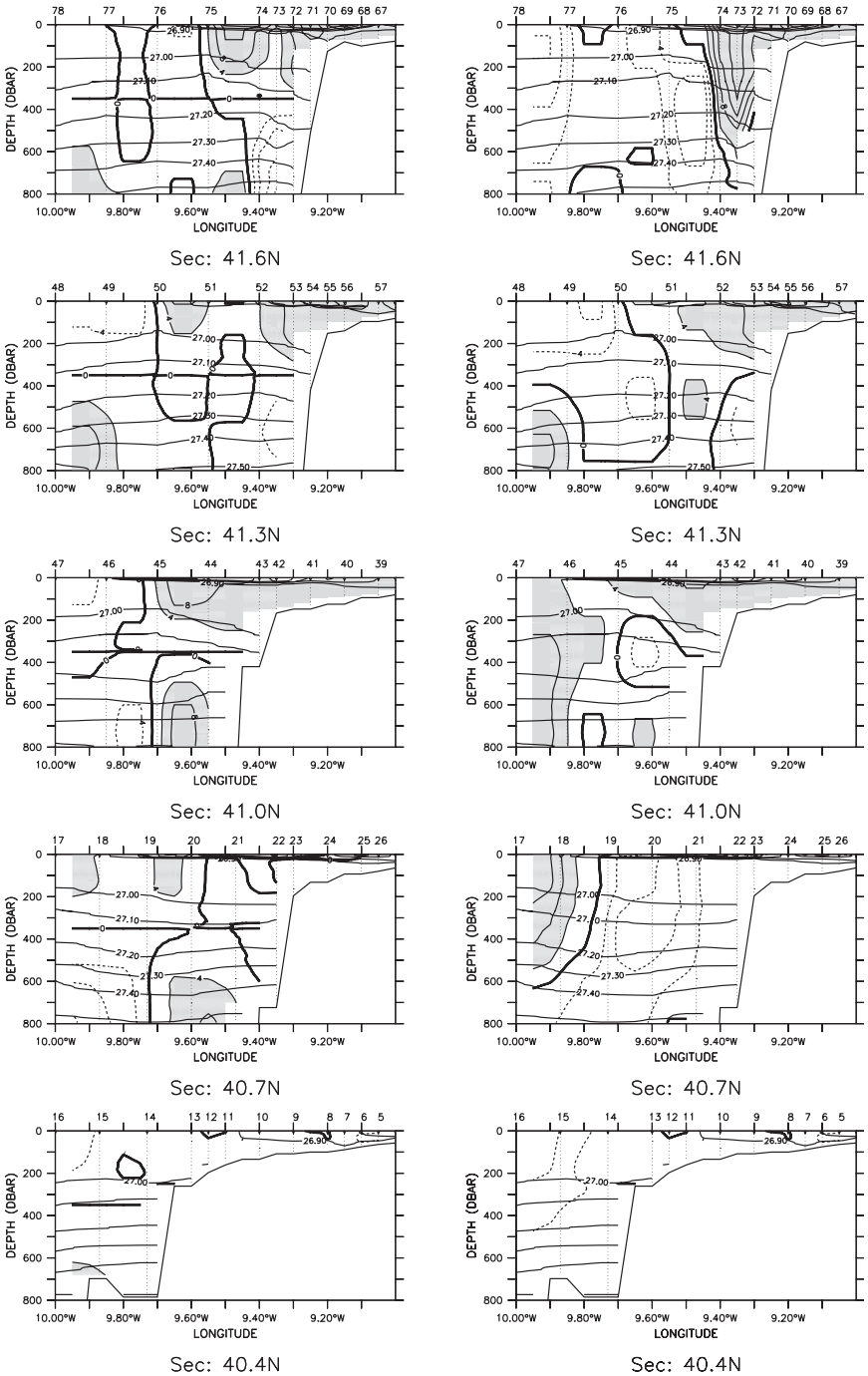

Fig. 6. Zonal section of meridional geostrophic velocity component using reference levels at 350 dbar (left) and 1400 dbar (right), superimposed in σ_θ contours. Shaded areas represent poleward flow with geostrophic velocities greater than 4 cm s^{-1}.

Table 1
Volume transports in Sv (10^6 m^3 s^{-1}) estimated from positive (poleward—Plwd) and negative (equatorward—Eqwd) meridional geostrophic velocity component using reference levels at 350 and 1400 dbar for the layers $\sigma_\theta < 27.0$ (surf.) and $27.0 < \sigma_\theta < 27.3$ (mid.)

Latitude	350 dbar ref.				1400 dbar ref.			
	Surf.		Mid.		Surf.		Mid.	
	Plwd	Eqwd	Plwd	Eqwd	Plwd	Eqwd	Plwd	Eqwd
41.6°N	0.6 0.4–0.8	0.1 0.0–0.3	0.2 0.0–0.7	0.2 0.0–0.7	0.6 0.5–0.8	0.3 0.2–0.5	0.3 0.2–0.6	0.9 0.5–1.5
41.3°N	0.6 0.3–0.9	0.2 0.0–0.4	0.2 0.0–0.8	0.1 0.0–0.6	0.6 0.3–0.8	0.3 0.1–0.4	0.2 0.1–0.6	0.4 0.1–0.8
41.0°N	0.6 0.3–1.0	0.1 0.0–0.2	0.2 0.0–0.6	0.1 0.0–0.5	0.7 0.3–1.1	0.0 0.0–0.0	0.6 0.3–1.0	0.1 0.0–0.3
40.7°N	0.2 0.1–0.6	0.0 0.0–0.3	0.1 0.0–0.6	0.1 0.0–0.5	0.3 0.2–0.4	0.5 0.2–0.8	0.3 0.2–0.5	0.7 0.4–1.1
40.4°N	0.0 0.0–0.2	0.3 0.0–0.7	0.0 0.0–0.2	0.0 0.0–0.2	0.0 0.0–0.0	0.5 0.2–0.8	0.0 0.0–0.0	0.2 0.1–0.4

The values presented beneath each estimate represent the range obtained by adding and subtracting 3 cm s^{-1} to the initial velocity values.

density distribution at 600 dbar presented in Fig. 4f, with a clearly identifiable anticyclonic eddy ($A1_{400}$), centered at 41°N, 9.7°W, where the relative minimum of the density field at 600 dbar is found. Northwest of this anticyclone the geostrophic flow is characterized by oppositely directed currents, displaying an anticyclonic rotation in the north ($A2_{400}$) and a cyclonic rotation in the west ($C1_{400}$), creating a confluence zone north of 41°N. North of 41.3°N, the geostrophic currents are southward to the west of 9.6°W, rotating northward and associated with a cyclonic feature located at about 9.4°W ($C2_{400}$).

At 100 dbar, four mesoscale features can also be identified in the map of the dynamic height referenced at 1400 dbar (Fig. 7b). In addition to the anticyclonic feature $A2$, there is another area where the geostrophic flow displays a clockwise rotation ($A1_{100}$), and two areas where the currents rotate cyclonically ($C1_{100}$ and $C2_{100}$). The identification of similar mesoscale structures at 100 dbar leads to the same generic description of the main flow paths and associated transports. However, since the structures are not found in exactly the same geographical positions, there are some changes in the position of some flow paths. In particular, concerning the resulting volume transports in the surface layer ($\sigma_\theta < 27.0$), the main consequence of the change in the position of the mesoscale structures is the increased poleward flow at 41°N and extinction of the equatorward flow at this latitude associated to a more southern position of anticyclone $A1_{100}$.

It should be stressed that the volume transport values presented in Table 1 should be regarded as first guesses taking into account the errors in the geostrophic velocity values as discussed above. However, from a careful evaluation of the range of values included in Table 1, combined with the dynamic height fields presented in Fig. 7, it is possible to draw schematic views of the non-divergent circulation at the mid-depth and surface layers in February 2000, as presented in Fig. 8. The values for the meridional volume transport were selected from the range of values presented in Table 1. The zonal transports were estimated assuming volume conservation between consecutive transects and no significant volume exchange between the shelf and slope regions.

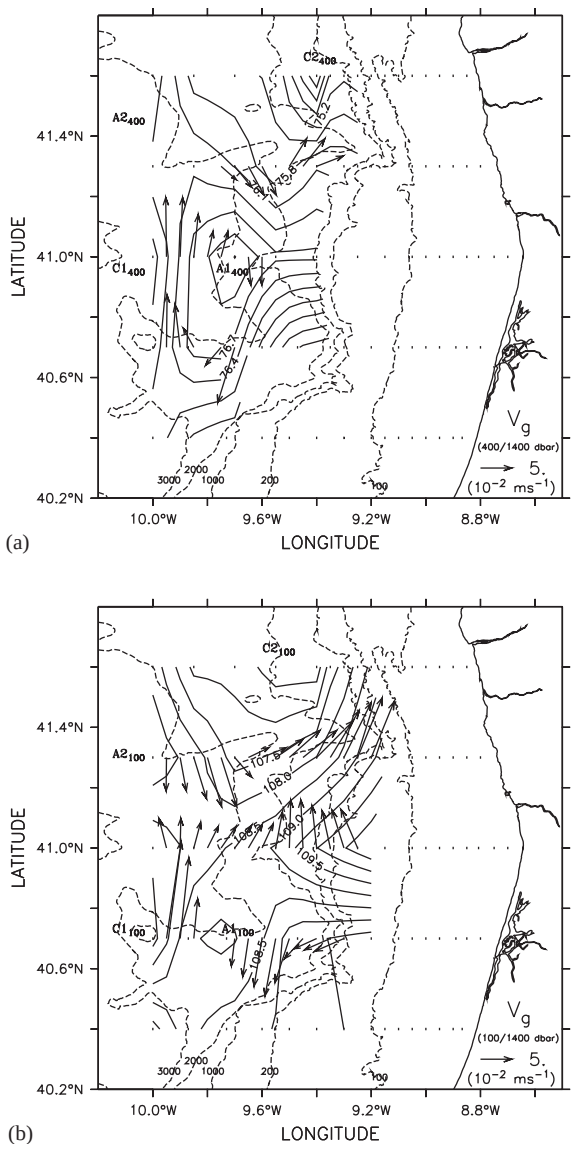

Fig. 7. Dynamic height (dyn cm) at 400 dbar (a) and 100 dbar (b) relative to 1400 dbar and geostrophic current vectors corresponding to velocities greater than 3 cm s^{-1}.

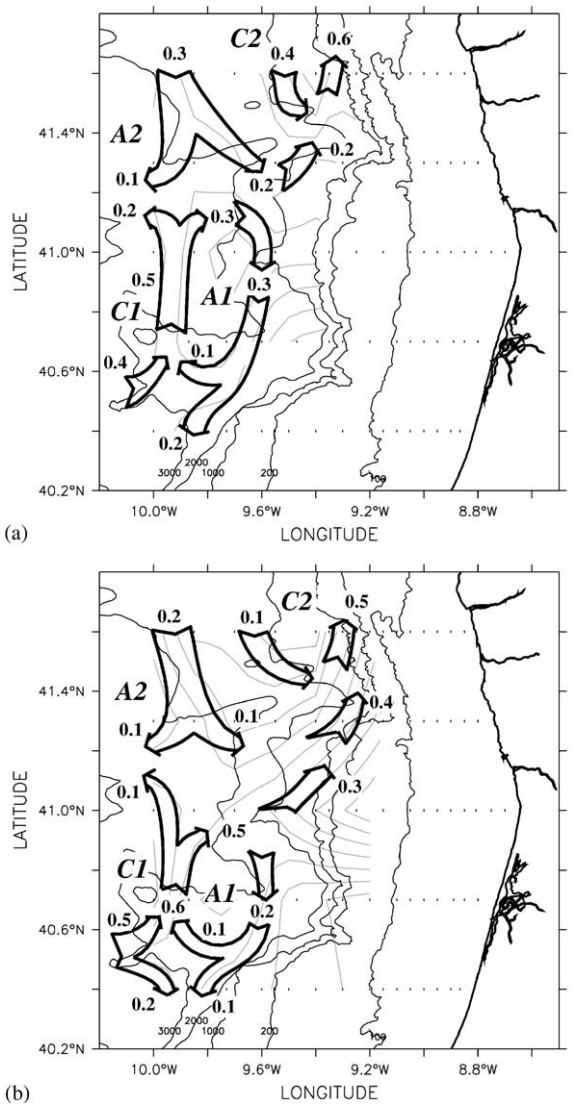

Fig. 8. Schematic views of the non-divergent circulation in the study region in February 2000, for two CW density layers: (a) $27.0<\sigma_\theta<27.3$ (mid.), (b) $\sigma_\theta<27.0$ (surf.). Eddy-like mesoscale structures with cyclonic and anticyclonic rotation are labeled as $C1/C2$ and $A1/A2$, respectively. The numbers associated with the main flow paths are volume transports in Sverdrup (10^6 m^3 s^{-1}).

From the relative position of the mesoscale structures and the volume transports in the mid-depth layer ($27.0<\sigma_\theta<27.3$) the following picture emerges: the poleward volume transport of 0.5 Sv at 40.7°N and 41°N takes place along the western side of the study region and is a result of an inshore flow of 0.4 Sv, entering the region between 40.4°N and 40.7°N, and the recirculation of 0.1 Sv along the southern sector of anticyclone $A1$. From the 0.5 Sv being transported poleward at 41°N, 0.2 Sv flows westwards leaving the surveyed area between 41°N and 41.3°N, while 0.3 Sv circulates along the northern and eastern sectors of

anticyclone $A1$. The equatorward flow in the near-slope region at 40.4°N appears as leakage of 0.2 Sv in the southern sector of anticyclone $A1$. About 0.7 Sv enters the study region through the northernmost section and follow two main paths. The offshore path transports 0.3 Sv southward and branches off before reaching the 41.3°N section, while 0.4 Sv recirculate cyclonically along the inshore path between 41.3°N and 41.6°N. The equatorward transport of 0.3 Sv at 41.3°N occurs along a clockwise turning offshore path associated to anticyclone $A2$, leading to an offshore transport of 0.1 Sv, and an inshore path associated to the southern sector of $C2$, responsible for the poleward transport of 0.2 Sv close to the slope at 41.3°N.

The main flow paths in the upper layer ($\sigma_\theta < 27.0$) are similar to the flow paths found in the mid-depth layer, being identifiable as the same mesoscale features. The most prominent difference between the circulation schemes presented in Fig. 8 is the poleward transport of 0.3 Sv in the near-slope region at 41°N, evidence of the continuity of the poleward flow in the upper layer, not found at mid-depth. This difference is linked to reduced meridional extension of $A1$ anticyclone and the flow branching in its northern sector between 40.7°N and 41°N.

It is important to note that the volume transport values presented in Fig. 8 were selected from the range of values presented in Table 1 which, in most cases, do not correspond to first-guess values. Moreover, it should be pointed out that the values at 40.7°N presented in Fig. 8 for equatorward volume transport in the mid-depth layer and the poleward volume transport in the surface layer are outside the range of values computed with the 1400 dbar reference level shown in Table 1. In the first case, the maximum value of 0.3 Sv flowing southward in the mid-depth layer at 41°N was selected because it was the closest to the range of values computed at 40.7°N (0.4–1.1 Sv), thus ensuring continuity in the equatorward flow. In the second case, a poleward flow of 0.6 Sv in the surface layer was found to be the minimum value to supply enough volume transport to feed the 0.4 Sv of poleward flow at 41°N and a minimum of 0.2 Sv southward return flow in the inshore region at 40.7°N. These discrepancies can be explained by the assumptions used to estimate the minimum and maximum values for the volume transports. Extreme values were computed assuming that all velocity profiles in each section are equally affected by the same error of $\pm 3\ \mathrm{cm\ s^{-1}}$; therefore, maximum (minimum) poleward (equatorward) transports were obtained when a value of $3\ \mathrm{cm\ s^{-1}}$ was added to all velocity profiles and minimum (maximum) poleward (equatorward) transports were obtained when a value of $3\ \mathrm{cm\ s^{-1}}$ was subtracted from all velocity profiles. However, the error in the geostrophic velocities changes along the section as shown in Fig. 5; therefore, the volume transport estimates are affected differently according to the position of the main flow paths.

4. Discussion and conclusions

The comparison between the geostrophic velocities obtained with different reference levels at 350 and 1400 dbar revealed significant changes in the vertical extension of the flow structures. In particular, the use of a reference level at 350 dbar introduces an artificial constraint to the vertical extent of the geostrophic flow and precludes the detection of a near-slope equatorward flow centered at 400 dbar. Although it is, to the authors' knowledge, the first time that the presence of a near-slope equatorward flow at depths close to 400 dbar has been inferred from field data, this is a common feature in numerical model simulations of the density-driven poleward slope current (Dubert, 1998; Peliz et al., 2003a, b). In particular, Peliz et al. (2003b) reported a weak undercurrent perturbed by the strong flow–topography interaction along the slope, but recurrent in all the simulations.

In February 2000, the circulation in the study region at CW levels was governed by a series of counter-rotating mesoscale features with length scales ranging from 10 to 60 km, leading to volume exchanges up to 0.5 Sv between the offshore and near-slope region in the upper CW layer ($\sigma_\theta < 27.0$) and about 0.3 Sv in the lower layer ($27.0 < \sigma_\theta < 27.3$). Although the circulation

patterns at the two CW layers reveal similar mesoscale features, the difference in their meridional extent leads to very significant changes in the integrated zonal volume transport of CW in the near-slope region. In particular, the reduction of the meridional extent of the anticyclonic eddy off the Aveiro Canyon (*A*1) in the upper layer, corresponds to a flow reversal between the two CW layers in the near-slope region at 41°N. The same volume transport of 0.3 Sv is estimated to flow poleward in the surface layer and equatorward in the lower layer; therefore, no net flow of CW is found near slope at this latitude when the two layers are added. In contrast, at the two northernmost sections the near-slope flow is directed poleward in both layers, with net poleward volume transports up to 1.1 Sv at 41.6°N for the whole CW layer. These results show that the deep signatures of the poleward current reported by Pérez et al. (2001) in the near-slope region in May 1993 depend on the vertical structure of the mesoscale eddies, which is strongly linked to the density distribution of the deeper layers. It should also be noted that the above results support the hypothesis of Pérez et al. (2001), who pointed to mesoscale eddies as the main mechanism for the downstream indirect ventilation of the upper CW layer. In particular, the presence of a near-slope equatorward flow in the lower CW layer opposing the poleward flow in the upper CW layer is probably very important in the meridional redistribution of the different modes of ENACW (cold/fresh in the North and warm/saltier in the south).

The above results clearly show the need for high-resolution sampling to be able to depict the main flow structures. Moreover, if the geostrophic currents are to be estimated by the dynamical method, it is necessary to know the density distribution down to depths below the Mediterranean Water influence (> 2000 dbar, say), given the very important vertical shears of the geostrophic currents down to those depths, and the impossibility of establishing a level of no motion in the upper layers. This must be taken into account in the design of field experiments using present-day technology, posing difficulties in reconciling survey synopticity and the time consumed in deep CTD casts. It is suggested that the best approach to study the circulation in the West Iberia CTZ is to use direct current measurements in conjunction with the hydrographic sampling.

In conclusion, the results presented here show that the winter poleward slope current observed off western Iberia, usually described as a narrow slope trapped flow structure, has a turbulent character with an associated mesoscale eddy field, corroborating previous studies based on field data (e.g., Fiúza et al., 1998; Pérez et al., 2001) and numerical models (Dubert 1998; Peliz et al., 2003b). Furthermore, the analysis of the vertical structure of the flow showed that much of the circulation in the upper CW layers is governed by the density distribution in the lower layers, indicating that for a better understanding of the circulation in the western Iberia CTZ further attention must be given to the coupling between Central and Mediterranean Water masses.

Acknowledgements

This work was supported by the project "SURVIVAL" (Assessing the Impact of Hydrodynamic Forcing on the Survival of Small Pelagic Fish Early Life Stages of Western Iberia) (FCT/PRAXIS/P/CTE/11282/1998). SURVIVAL is a project affiliated to GLOBEC (SCOR/ICSU/IOC) and the PELAGICOS Programmes (FCT/IPIMAR).

The authors wish to acknowledge the use of the Ferret program for analysis and graphics in this paper. Ferret is a product of NOAA's Pacific Marine Environmental Laboratory (information is available at www.ferret.noaa.gov).

References

Ambar, I., Fiúza, A., 1994. Some features of the Portugal Current System: a poleward slope undercurrent, an upwelling-related summer southward flow and an autumn–winter poleward coastal surface current. In: Katsaros, K., Fiúza, A., Ambar, I. (Eds.), Proceedings of the Second International Conference on Air–Sea Interaction and on Meteorology and Oceanography of the Coastal Zone. American Meteorological Society, Lisbon, Portugal, pp. 286–287.

Ambar, I., Howe, M., 1979. Observations of the Mediterranean outflow: I. mixing in the Mediterranean outflow. Deep Sea Research 26A, 535–554.

Barton, E., 1998. Eastern boundary of the North Atlantic: Northwest Africa and Iberia. Coastal Segment (18,E). In: Robinson, A.R., Brink, K.H. (Eds.), The Sea, Vol. 11. Wiley, New York, pp. 633–657.

Dubert, J., 1998. Dynamique du Système de Courants vers le Pôle au Voisinage de la Pente Continentale à l'Ouest et au Nord de la Péninsule Ibérique. Ph.D. Thesis, University of Bretagne Occidentale, available from the Department of Physics, University of Aveiro, Portugal.

Fiúza, A., Sousa, F., 1989. Preliminary results of a CTD survey in the Coastal Transition Zone Off Portugal during 1–9 September 1988. The CTZ Newsletter, 4(1), 2–9.

Fiúza, A., Hamman, M., Ambar, I., Díaz del Río, G., González, N., Cabanas, J., 1998. Water masses and their circulation off western Iberia during May 1993. Deep-Sea Research I 45, 1127–1160.

Fofonoff, N., Millard, R., 1983. Algorithms for computation of fundamental properties of seawater. UNESCO Tech. Pap. Mar. Sci. vol. 44, UNESCO, Paris, 53pp.

Frouin, R., Fiúza, A., Ambar, I., Boyd, T., 1990. Observations of a poleward surface current off the coasts of Portugal and Spain during winter. Journal of Geophysical Research 95 (C1), 679–691.

Haynes, R., Barton, E., 1990. A poleward flow along the Atlantic coast of the Iberian Peninsula. Journal of Geophysical Research 95, 11425–11441.

John, H.-C., Ré, P., Zuelicke, C., 1996. Sardine larvae in a spring-upwelling event off northern Portugal. Ciência Biológica Ecology and Systematics 16, 193–198.

Mazé, J., Arhan, M., Mercier, H., 1997. Volume budget of the eastern boundary layer off the Iberian Peninsula. Deep-Sea Research I 44 (9–10), 1543–1574.

Oliveira, P., Serra, N., Fiúza, A., Ambar, I., 2000. A study of meddies using simultaneous in-situ and satellite observations. In: Halpern, D. (Ed.), Satellites, Oceanography and Society. Elsevier Science B.V., Amsterdam, pp. 125–148.

Peliz, A., Dubert, J., Haidvogel, D., 2003a. Subinertial response of a density driven Eastern Boundary Poleward Current to wind forcing. Journal of Physical Oceanography 33, 1633–1650.

Peliz, A., Dubert, J., Haidvogel, D., Le Cann, B., 2003b. Generation and unstable evolution of a Density-Driven Eastern Poleward Current. Journal of Geophysical Research 108 (C8), 3268 doi:10.1029/2002JC001443.

Peliz, A., Rosa, T., Santos, A., Pissarra, J., 2002. Fronts, jets, and counter flows in the Western Iberian upwelling system. Journal of Marine Systems 35, 61–77.

Pérez, F., Castro, C., Álvarez-Salgado, X., Ríos, A., 2001. Coupling between the Iberian basin–scale circulation and the Portugal boundary current system: a chemical study. Deep-Sea Research I 48, 1519–1533.

Pingree, R., 1995. The droguing of meddy Pinball and seeding with ALACE floats. Journal of the Marine Biological Association of the UK 75, 235–252.

Pingree, R., Le Cann, B., 1993. A shallow meddy (a smeddy) from the secondary mediterranean salinity maximum. Journal of Geophysical Research 98 (C11), 20169–20185.

Reid, J., Mantyla, A., 1976. The effect of the geostrophic flow upon coastal sea elevations in the northern north Pacific ocean. Journal of Geophysical Research 81 (18), 3100–3110.

Ríos, A., Pérez, F., Fraga, F., 1992. Water masses in the upper and middle North Atlantic Ocean east of the Azores. Deep-Sea Research 39, 645–658.

Santos, A., 2000. The SURVIVAL'2000 cruise: first results. Globec International Newsletter 6 (2), 5–6.

Santos, A.M.P., Peliz, A., Dubert, J., Oliveira, P.B., Angélico, M.M., Ré, P., 2004. Impact of a winter upwelling event on the distribution and transport of sardine eggs and larvae off western Iberia: a retention mechanism. Continental Shelf Research 24, 149–165.

Stammer, D., Hinrichsen, H.-H., Käse, R., 1991. Can meddies be detected by satellite altimetry? Journal of Geophysical Research 96 (C4), 7005–7014.